

Morphological and Local Mechanical Surface Characterization of Ballistic Fibers via AFM

Kenneth E. Strawhecker,¹ Daniel P. Cole²

¹U.S. Army Research Laboratory, RDRL-WMM-G, Aberdeen Proving Ground, Maryland 21005-5069

²U.S. Army Research Laboratory, RDRL-VTM, Aberdeen Proving Ground, Maryland 21005-5069

Correspondence to: K. E. Strawhecker (E-mail: kenneth.e.strawhecker.civ@mail.mil)

ABSTRACT: As-received morphologies, defect structures, and contact moduli of Kevlar KM2 Plus and three other ballistic fibers varying in chemistry and processing, were observed and compared using atomic force microscopy (AFM) and instrumented nanoindentation (NI) techniques. Surface features and defects were defined and measured for each fiber chemistry: *p*-phenylene terephthalamides (PPTA including KM2 Plus and Twaron), co-polymer aramid (AuTx), and ultra high molecular weight polyethylene (UHMWPE including Dyneema). Although a multitude of surface defects were observed in each fiber, the types of defects were similar from one fiber type to another. It was found that surface defects generally map to a more compliant local modulus value. Contact modulus values were compared with NI elastic modulus values to demonstrate validity for the AFM technique. Challenges and limitations of the AFM technique for cataloging defects are discussed. This study is the first which attempts to outline the various morphologies found on several fiber surfaces. These local property studies will enable future comparisons with single filament and bulk fiber properties. © 2014 Wiley Periodicals, Inc. *J. Appl. Polym. Sci.* **2014**, *131*, 40880.

KEYWORDS: fibers; mechanical properties; morphology; properties and characterization; structure-property relations

Received 25 February 2014; accepted 17 April 2014

DOI: 10.1002/app.40880

INTRODUCTION

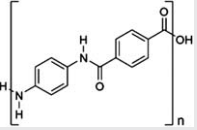
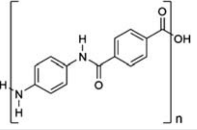
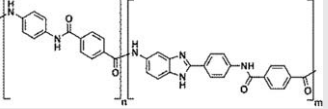
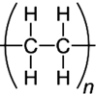
Ballistic fiber properties, such as tensile modulus and tensile strength, may be varied through chemistry and processing. These fiber properties are related to the overall ballistic performance (V50) of a fabric.^{1–5} The same property/performance relationships are applicable to ballistic fiber composite materials.^{1,4} These studies partially define how to improve ballistic performance based upon fiber properties. Improvement of fiber properties, then, is a good starting point for improving ballistic performance. Morphology and structure on a more local scale are related to individual filament properties. Therefore, it is also important to understand hierarchical relationships from local to single filament fiber properties, which are related through the nano- to micro-scale morphology within the single fiber or filament. Many studies conclude that, in general, differences in architecture and morphology can arise due to chemistry and processing differences.^{6–21} These studies utilize various methods of investigation and include different classes of chemistry, namely ultrahigh molecular weight polyethylene (UHMWPE),^{6,11–13,17,18,21} poly(para-phenylene terephthalamide) (PPTA),^{7–10,14,15,20} and PPTA copolymers.^{16,19} Therefore, it is also relevant to define and understand the anatomy of these fiber surfaces across these length scales, especially considering the role that these morphological features

may play in the integrity of the filament as it is mechanically loaded.

Popular choices for ballistic fiber chemistries include PPTA (such as Kevlar and Twaron), PPTA copolymers (such as AuTx), and UHMWPE (such as Dyneema and Spectra fibers). The structures of these molecules are shown in the schematic, Table I. The repeat unit in PPTA accounts for the Twaron and the KM2 fibers. The PPTA structure is linear. The repeat unit used in the AuTx fiber is slightly bent as shown in Table I. Dyneema structure is linear and possesses a relatively simple repeat unit, compared with the other fibers tested in this study.

Several studies have been performed in order to understand the effect of defects on the properties of specific fibers of interest.^{22–29} Additionally, multiple researchers have investigated the effects of drawing, draw-ratio, and spin-speed of UHMWPE fibers on the morphology and the resultant properties.^{6,11–13,17,18,21} These studies show that there is a difference in high strain rate versus quasistatic behavior for UHMWPE fibers and the data suggest that the difference lies in the reorganization of the structure of the UHMWPE, especially with respect to amorphous versus crystalline regions. These studies focus on the general effect of increasing the likelihood of a defect on the overall mechanical properties. The model suggests that morphologies

Table I. Properties of Fibers Used in this Study

Fiber	Chemical structure	Contact modulus (GPa)	Radial indentation modulus (GPa)
KM2 Plus		4.46 ± 1.49	5.92 ± 0.63
Twaron		3.03 ± 1.32	5.92 ± 1.36
AuTx		3.44 ± 2.88	5.28 ± 0.60
Dyneema		2.26 ± 1.88	3.61 ± 0.71

dictate properties through critical defects. A critical defect may have a certain minimum size and corresponding local properties. Furthermore, the density of critical defects—or distance between critical defects—is an important parameter. The evidence for this stems from reduced testing volumes containing presumably less critical defects. In the works mentioned, failure surfaces were analyzed to understand the fracture mechanisms. What remains to be studied is the detailed effect of these as-received morphologies and the defects therein as they pertain to fiber properties. It would be valuable to determine if surface defects ultimately lead to failure when a fiber is strained. Even more valuable would be the ability to identify these specific defects with respect to their size and origin.

To that end, this study employs atomic force microscopy (AFM)-modulus mapping techniques in order to qualitatively illustrate and also quantify local surface morphologies of filaments with respect to roughness and stiffness. The AFM contact modulus mapping depends upon very accurate knowledge of tip size and shape as well as accurate control of contact depth (or contact area). Because of these limitations, the contact modulus values were also compared with mechanical properties of single filaments found through instrumented indentation. The observations shown here may lead to a better understanding of the effect of chemistry and processing on the morphologies and fiber properties, and ultimately on ballistic performance.

EXPERIMENTAL

Materials

The four different ballistic fibers (listed in Table I, along with properties to be described) used in this study were obtained from Natick Soldier Research, Development & Engineering Center (Natick, MA 01760-5000). Individual fibrils were teased from the tows and used as received. Two of these fiber types possessed the poly (*p*-phenylene terephthalamide) (PPTA)

chemistry: KM2 Plus (600 denier), and Twaron OP25 (500 denier). The Russian copolymer, AuTx (265 denier), with PPTA-poly (benzimidazole) chemistry, was also tested. In addition, ultra high molecular weight polyethylene (UHMWPE) fibers were tested: Dyneema SK76 (1350 denier). For the purposes of this work, the materials will be referred to as: KM2 Plus, Twaron, AuTx, and Dyneema.

AFM

AFM-modulus imaging was utilized in this study. Imaging was performed using a MultiMode8 AFM with a Nanoscope V controller using PeakForce Quantitative Nanomechanical Mapping (PF QNM) mode. Commercial AFM tips including TAP150A, FESPA and TESPA (Bruker), and AC200TS (Asylum Research), were used as received. Contact modulus map images were obtained using the relative method described elsewhere.³⁰ The reference sample employed for this method was a spin-cast polystyrene (PS) film sample from Bruker-Nano, which has a reported modulus of 2.7 GPa. Elastic modulus, or, contact modulus was determined using the PS as a reference and the PF QNM method, which uses the Derjaguin–Muller–Toporov (DMT) modulus model.³¹ DMT contact modulus values were obtained without modification to images.

To obtain representative surface morphologies, single filaments were selected at random from a tow and fixed to double-sided adhesive on metal pucks for AFM analysis. Not only were several fibers scanned, but each fiber was scanned in multiple locations, with the goal of capturing the true character of the filament surface morphology. Additionally, the tests were repeated, where for each fiber type, new filaments were chosen and tested on different occasions using different probes.

In order to measure quantitative values for the local modulus, first the average value over all pixels in a given image was evaluated. Then, features within the images were selected for local

modulus evaluations. A digital zoom was performed within the image followed by a manual outlining of the feature(s) of interest. Typically, 5–10 such regions were measured and averaged. These defect region moduli are reported herein in quantitative fashion either as the number or as a percentage change from the full given image average.

Instrumented Nanoindentation (NI)

Samples were prepared for instrumented indentation using a previously reported fiber mounting technique.³² Briefly, 1 g washers were attached to the ends of a single fiber and the samples were suspended over a glass vial shell (Thomas Scientific). The fibers were mounted to the shells with two small drops of adhesive (Loctite 416) approximately 5–7 mm apart, centered on the shell apex, which ensured sufficient fiber–substrate contact for indentation. Instrumented indentation tests were performed using a Hysitron TI-950 TriboIndenter with a diamond Berkovich tip (radius of curvature ~ 100 nm). Indentation areas at least $50\mu\text{m}$ away from the fiber–adhesive interface were targeted using the optical microscope in the TriboIndenter. Measurements were performed in displacement control mode, with a maximum indent depth of approximately 200 nm. A triangular force profile was employed, using a quasi-static loading rate of 25 nm s^{-1} . For each fiber, a minimum of five measurements were made along the sample, spaced a minimum of $5\mu\text{m}$ from subsequent indents. For each fiber type (KM2 Plus, Twaron, AuTx, Dyneema), three separate single fibers were tested, which provided a minimum of 15 measurements per sample type. Elastic modulus values in the fiber radial direction (NI-OP) were approximated by applying the Oliver–Pharr (OP) method, which assumes the samples are isotropic, semi-infinite half spaces.³³ To obtain sample properties, the elastic modulus and Poisson's ratio of the probe were assumed to be 1140 GPa and 0.17, respectively, and a value of 0.33 was assumed for the Poisson's ratio of the sample.³³

RESULTS AND DISCUSSION

AFM Modulus Mapping of Fiber Surfaces

AFM was performed on the free surface of four as-received ballistic fibers to investigate the morphology as a function of processing and chemistry, and to provide a basis for understanding how individual filament morphology relates to ultimate fiber properties. The approach taken is to first observe the KM2 Plus morphology in qualitative detail in order to describe the various types of defects and other fiber features. The KM2 Plus morphology is then qualitatively compared and contrasted to the other three fibers. Next, the local modulus values are quantified for each fiber type and compared with single filament indentation data. Data reliability with respect to AFM methods is discussed. Finally, the results lead to a discussion of how the data can be applied to understand single filament behavior and fiber properties, such as tensile strength or tenacity.

To gain perspective on the various scan sizes that will be examined, Figure 1 shows a $6\mu\text{m}$ scan three-dimensional (3D) perspective view of a single KM2 Plus fiber. The image is a height, (topography) scan only. *In all of the images presented here, the scan direction is across the fiber cylinder—that is, at 90° to the fiber axis direction.* Note the curved semi-cylindrical surface in

Figure 1. The KM2 Plus cylindrical surface seen here is similar in overall shape to the Twaron and AuTx, but differs slightly from the overall Dyneema which maintains a long-range corrugated roughness and reduces the curvature found in many images. The extent to which the overall cylindrical shape is present in these fibers is not as crucial to this study as the detailed morphologies found on the filament surfaces. Therefore, to see better detail in the images, two-dimensional (2D) renderings of the height will be shown, where a second-order plane-fit routine has been applied to the data to remove the cylindrical shape.

KM2 Plus Fiber Surface Morphology

In order to highlight one of the largest types of features found in these fibers before plane-fitting, it is important to note whether the region shown is cylindrical or contains a flat edge from processing. Inspection of Figure 1 shows that there is a flat edge on the left side of the fiber, becoming more prominent toward the top of the scanned region (i.e., running from the bottom-center corner of the perspective view of Figure 1 to the top-left corner). This flat region was observed in approximately 50% of the KM2 Plus fibers examined in this study.

For a better overview of filament morphologies, regions much larger than the features must be surveyed such that: (1) defects can be defined, and (2) defect contribution to local properties can be quantified. Figures 2 and 3 are collections of KM2 Plus feature regions. Figure 2(a) is the 2D rendering of Figure 1. Figure 2(b) is the simultaneously captured accompanying modulus data. What is readily apparent in these images is a long stray or pulled-out fibril or bundle of fibrils measuring approximately 26 nm tall by 100 nm wide (note: there is a tip broadening effect with AFM measurements, the height is less sensitive to this effect) stretching across the image. This bundle appears in the zoom image of Figure 2(d) to be 20% lower in modulus value than the image as a whole.

Figure 2(c) (height) and 2(d) (modulus) show not only more detail on the stray fibril but also capture tiny pores (20–50 nm diameter, at least 5–10 nm deep) surrounded by disrupted fibrillar regions [most prominently in the upper right quadrant, Figure 2(c)], long scratches or trenches [50 nm wide; one of these nearly dissects Figure 2(c), and there are at least three of these features in Figure 2(a)], raised bumps of random shape, location, and size (30–90 nm wide and 15–30 nm tall), and also larger raised features of odd shapes, possibly an agglomeration of many of the raised bumps—which is surmised solely upon the fact that the modulus recorded in Figure 2(b,d) for both the raised bumps and the raised odd shapes appears to be similar and well below the image average. (The raised bumps average 1.95 versus 5.16 GPa for the entire image, a 62% decrease.) On the other hand, the scratches and disruptions show only a slight decrease in modulus, but upon further inspection, the matching features in the modulus image (scratches and disruptions) were almost always offset, suggesting that the shading is a result of a topographical artifact—where either the tip experiences a different contact area when it is touching the side of a raised feature or the walls of a sunken feature, such as a trench. (Since this behavior is non-trivial and related to scan direction, feature

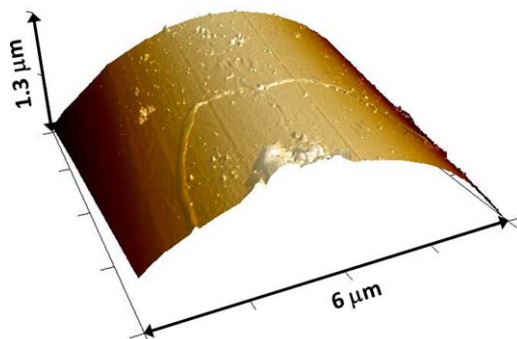


Figure 1. $6 \times 6 \mu\text{m}$ AFM 3-D view of KM2 Plus showing the cylindrical shape of the fiber. [Color figure can be viewed in the online issue, which is available at wileyonlinelibrary.com.]

direction, and also the size of the tip with respect to the feature, it is not possible to correlate all features with scan direction and so the specific solutions are left to a future study.) Finally, appearing in Figure 2(c) are many regions or small islands of raised haze which could be attributed to stray fibrils, specifically: not bundles, but single or small groups of fibrils. There appears to be a half-micron strip of this haze running top to bottom on the left side of Figure 2(c), indicated by the arrows. Furthermore, a similar raised feature surrounds the pores that were previously identified. Additionally, there is a larger scratch-like feature (800 nm long by 200 nm wide, triangular shaped, pointing toward the top of the image), possibly a larger pore, partially covered by the large pulled-out fibril bundle in the lower right quadrant of Figure 2(c). This larger scratch-like

feature is surrounded by the haze of presumably stray fibrils. Moving further from these regions of haze toward the center of the image, it is possible to see various placements of these solo stray fibrils. This arrangement suggests that the stray fibrils may be tethered at one end to the surface and that the disruption occurs in concert with other, larger defects. The stray fibrils do not seem to play a role in the local modulus values, but it is possible that these are ubiquitous and therefore part of the inherent surface stiffness.

Figure 3 is a zoom series of a KM2 Plus fiber region with many of the same types of features. Each of the four height/modulus (left/right) pairs in Figure 3 is a separate scan performed in order to observe each of the defects at higher resolution. Moving from top to bottom in this series, Figure 3(a) exhibits long scratches and trenches running the length of the scan, with raised bumps and collections of raised bumps most prominent in the center of the image. As before, the raised bumps possess a relatively low modulus with respect to the image average [bumps in Figure 3(f) are 2.55 GPa, a 57% decrease from the image modulus of 5.74 GPa]. The left side of Figure 3(e) appears to be shaded to lower stiffness values in general, but this behavior is noted on most of the larger scans in this study and is due to the changing tip-sample contact area as the tip moves away from the top of the fiber. This is a subject of ongoing study and will be addressed to some extent in a later section. (Because of this imaging artifact which occurs on larger scans, images investigated in this study are primarily 3 microns or less, except where specifically noted, and only because the larger morphological features warrant such scan sizes.)

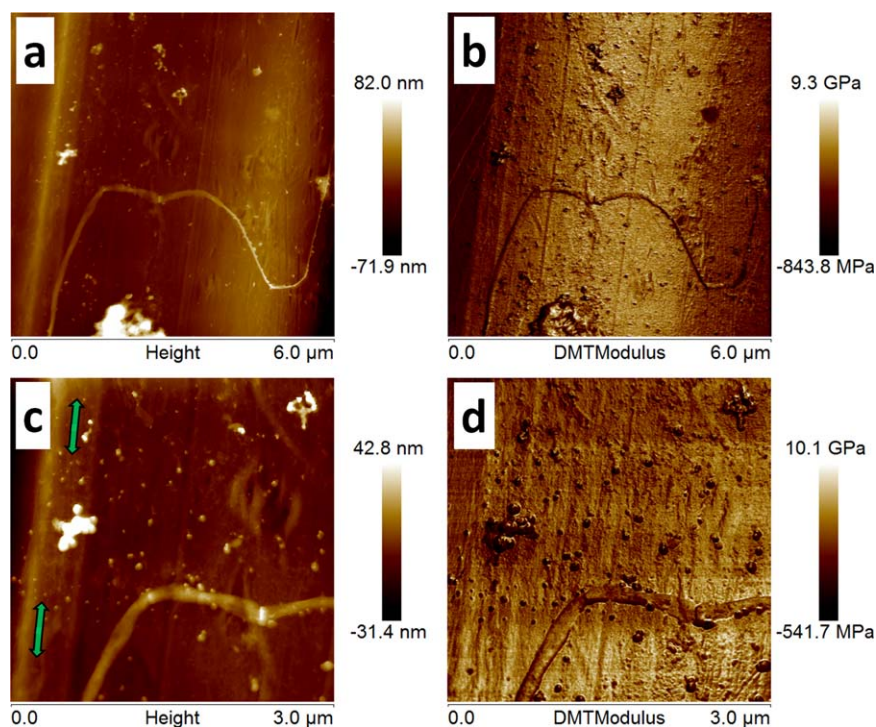


Figure 2. $6 \times 6 \mu\text{m}$ (top) and $3 \times 3 \mu\text{m}$ (bottom) AFM topography (a,c) and DMT contact modulus (b,d) images showing typical surface defects found on as-received KM2 Plus fiber surfaces. Figure 2(a) is the same as Figure 1, second order plane-fitted. [Color figure can be viewed in the online issue, which is available at wileyonlinelibrary.com.]

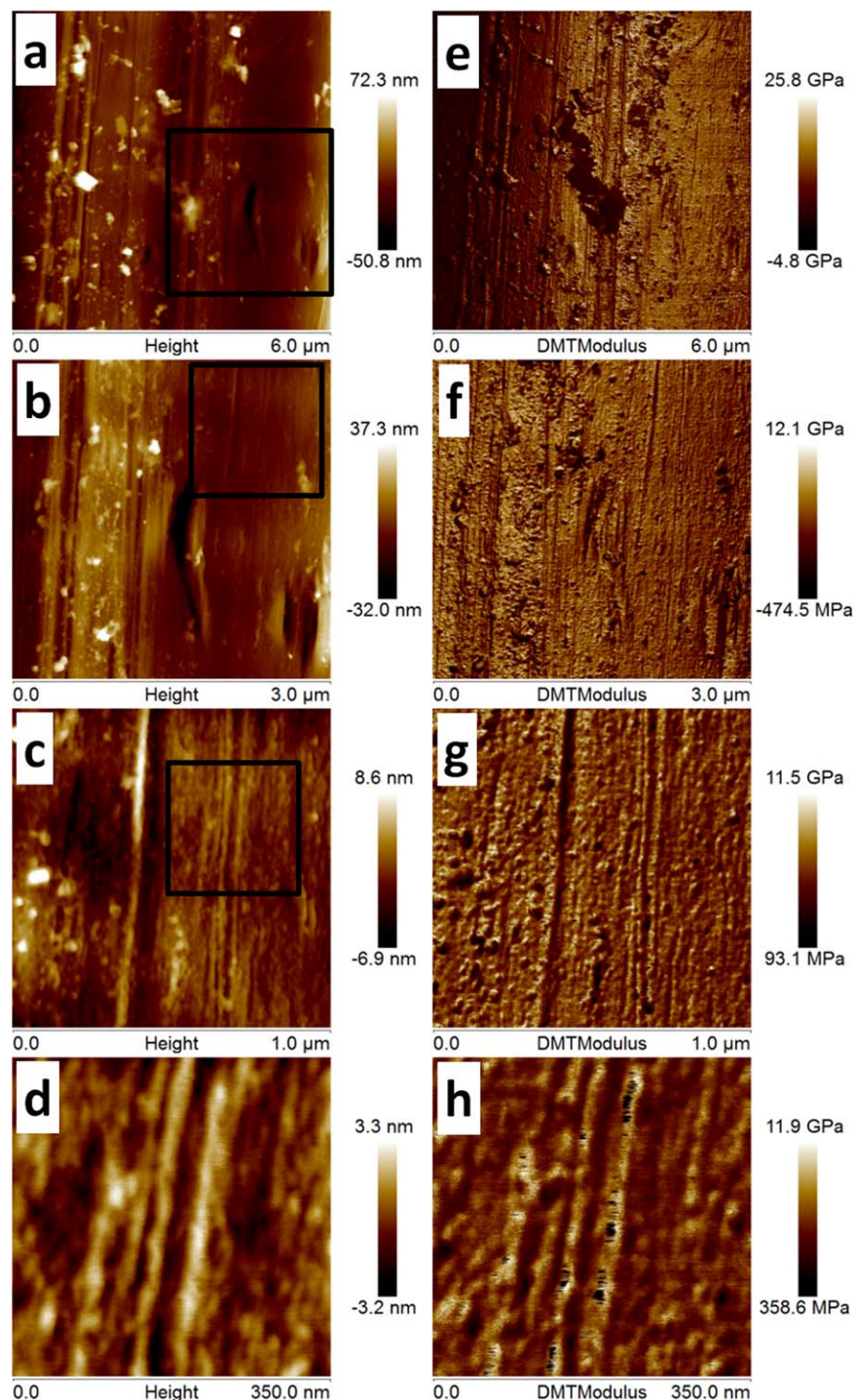


Figure 3. KM2 Plus zoom series (top to bottom: $6 \times 6 \mu\text{m}$, $3 \times 3 \mu\text{m}$, $1 \times 1 \mu\text{m}$, and $350 \times 350 \text{ nm}$) AFM topography (a–d) and DMT contact modulus (e–h) images showing typical surface defects found on as-received KM2 Plus fiber surfaces. [Color figure can be viewed in the online issue, which is available at wileyonlinelibrary.com.]

Also found in Figure 3(a) is a region with concentrations of disrupted fibrillar regions or (larger and smaller) scratch-like features. Figure 3(b,f) show enhanced detail of these features, which could be either short scratches or pores, as identified in Figure 2. As discussed previously, the modulus image primarily shows the large contrast only for the raised bumps, while small contrasts are present for the fibril and long-scratch types of fea-

tures that run top-to-bottom. Figure 3(c,g) are $1 \mu\text{m}$ scans that show a portion of the fiber surface that is relatively defect-free. While there is still a long-scratch and a few raised bumps plus a small pore, it is possible to see the morphology that was apparently intended for KM2 Plus fibers: fibrils or bundles of fibrils running top-to-bottom and relatively undisrupted. This is shown in highest resolution in Figure 3(d,h).

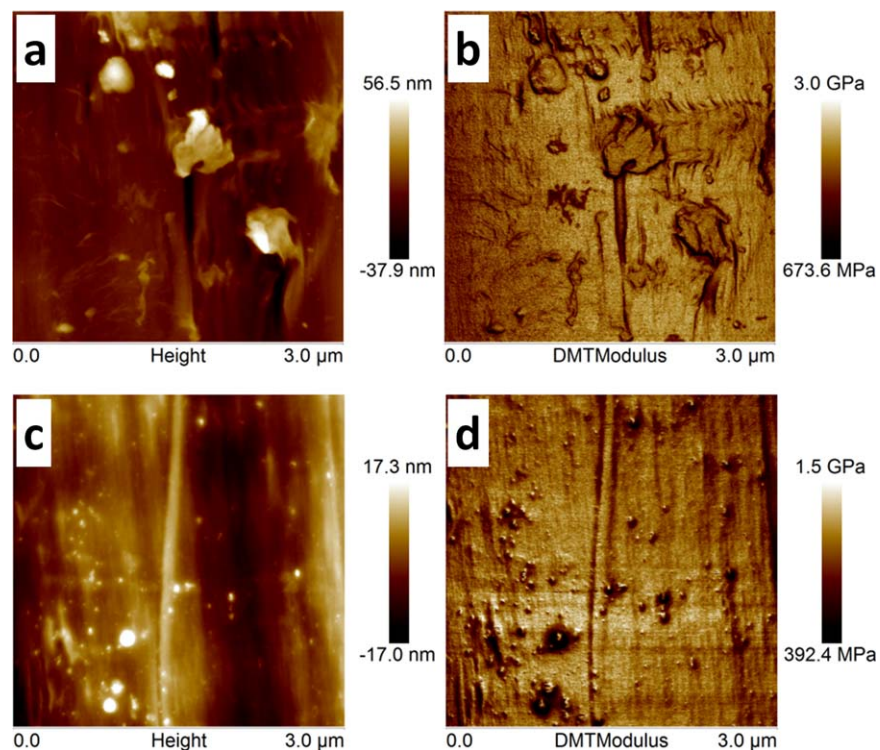


Figure 4. $3 \times 3 \mu\text{m}$ AFM topography (a,c) and DMT contact modulus (b,d) images showing typical surface defects found on as-received Twaron fiber surfaces. [Color figure can be viewed in the online issue, which is available at wileyonlinelibrary.com.]

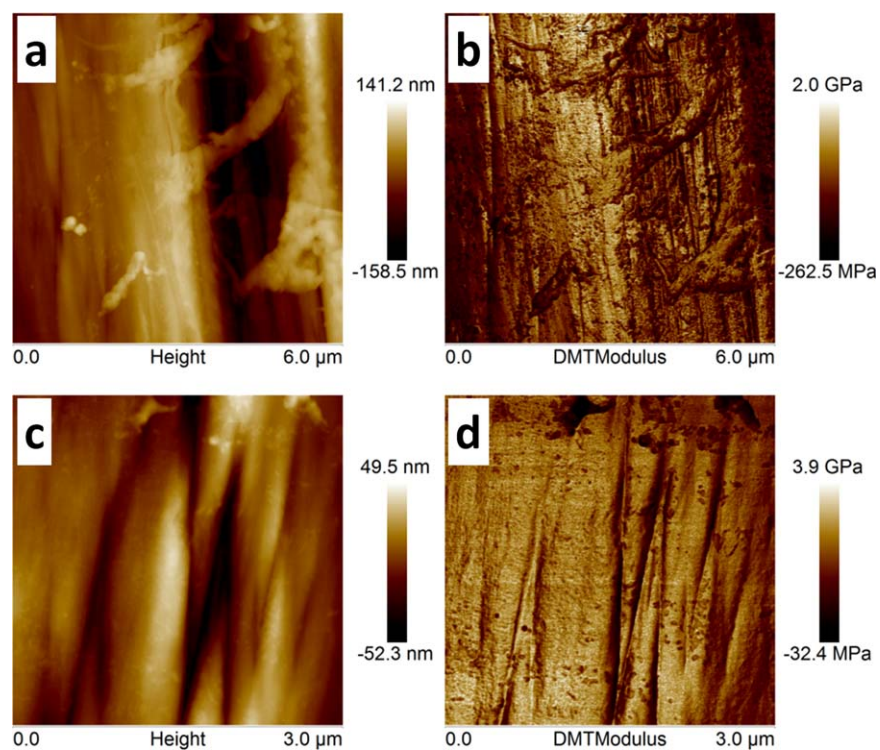


Figure 5. $6 \times 6 \mu\text{m}$ (top) and $3 \times 3 \mu\text{m}$ (bottom) AFM topography (a,c) and DMT contact modulus (b,d) images showing typical surface defects found on as-received AuTx fiber surfaces. [Color figure can be viewed in the online issue, which is available at wileyonlinelibrary.com.]

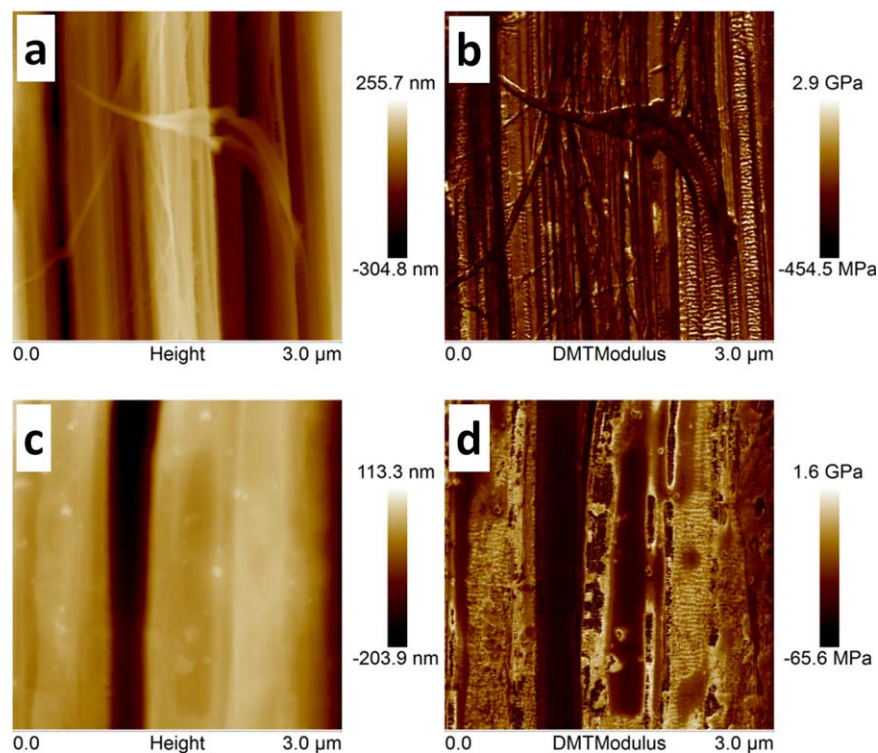


Figure 6. $3 \times 3 \mu\text{m}$ AFM topography (a,c) and DMT contact modulus (b,d) images showing typical surface defects found on as-received Dyneema fiber surfaces. [Color figure can be viewed in the online issue, which is available at wileyonlinelibrary.com.]

Twaron, AuTx, and Dyneema Fiber Surface Morphology

The description of the KM2 Plus surface morphology above provides a foundation for describing the other ballistic fibers. For the most part, features will remain the same and the corresponding effect on the local modulus will be similar. Therefore, a cursory look at each of the three remaining fibers will be shown, with comparison and contrast to KM2 Plus, followed by a comparison of the overall modulus values obtained from AFM modulus images. The results will then be compared with the mechanical properties of the fibers obtained through NI.

Prior to plane fitting corrections, Twaron filaments appear cylindrical but may in some cases have a flat side similar to the KM2 Plus fibers, due to the processing conditions. Figure 4 includes two pairs of $3 \times 3 \mu\text{m}$ images of a Twaron filament. Figure 4(a,b) show three notable features: larger scratch-like features, comparable to those found in Figure 3(a,b) (25 nm deep, 130 nm wide), heaps or clusters of material appearing to have come out of the trenches (35 nm tall and 400 nm diameter), and stray fibrils (2–5 nm tall and 250–500 nm long). Figure 4(c,d) add a long stray or pulled-out fibril or bundle of fibrils (10 nm tall and 100 nm wide, running the length of the image), and raised bumps of random size and shape (10–15 nm tall and 50–60 nm diameter), all similar to features found in Figures 2 and 3. Interestingly, the raised bump features appear to be stiffer than the matrix, although surrounded by a compliant corona [Figure 4(d)]; however, this type of feature could be an artifact of the topography. In slight contrast to the KM2 Plus, it appears that some of the scratch-like features found in the Twaron [Figure 4(a,b)] have a lateral dimension, where the fibril disruption seems to have a left–right direction. In all cases of

these features [except the very long fibril bundle of Figure 4(c,d)], the modulus image shows a slight decrease in the stiffness in each defect region. In Figure 4(c,d), it is possible to see the fine fibrillar structure that was intended for the Twaron fiber.

Filament surfaces of the AuTx fiber are roughly cylindrical before plane-fitting, but a corrugated, braided roughness is prominent even before this correction. Figure 5 includes two pairs of images (5a and 5b: $6 \times 6 \mu\text{m}$, 5c and 5d: $3 \times 3 \mu\text{m}$) of the AuTx filament surface. (Note that the relative sizes of the features found in the AuTx filament surface, with respect to the other filament features in this study, warrant the inclusion of these larger, 6 micron scan ranges. Therefore, it is important to keep in mind that the edges of the 6 micron scans usually contain an apparent-lower-modulus artifact which is discussed in a later section.)

Figure 5(c,d) show primarily large fibril bundles which are not pulled-out, but rather appear to be braided. There is a scratch or lateral disruption across three of the bundles, at about 1 micron down from the top of the image. Close inspection proves that these are bundles of fibrils, as it can be observed that the disruption is actually many fibrils that are becoming separated from one another. Also, at the very top of Figure 5(c,d), there are raised bumps (primarily clustered) which map to a much lower measured stiffness value—clusters 70% less and single bumps 44% less—than the overall image (5d modulus, 2.14 GPa). Figure 5(a,b) ($6 \times 6 \mu\text{m}$) show many long stray or pulled-out fibrils or bundles of fibrils whose ends appear to have been pulled laterally across the fiber surface. Figure 5(a,b)

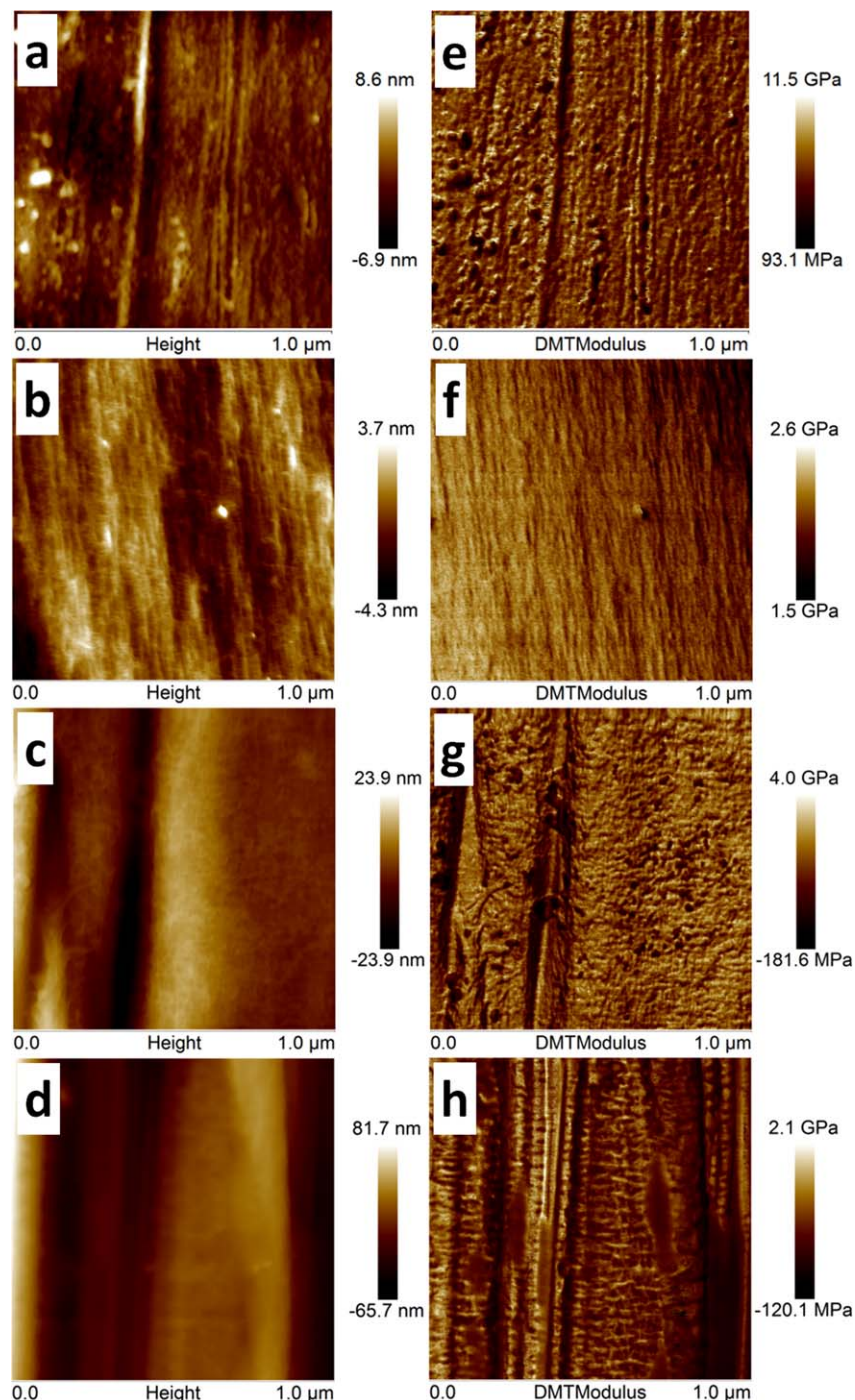


Figure 7. Atomic force microscope surface topography (a–d) and modulus maps (e–h) of as-received ballistic fibers used in this study. (a,e) KM2 Plus, (b,f) Twaron, (c,g) AuTx, and (d,h) Dyneema. Regions detailed are expected, routine fiber surfaces with few flaws. [Color figure can be viewed in the online issue, which is available at wileyonlinelibrary.com.]

also exhibit a large population of raised bumps which map to 40%–50% lower stiffness. Also apparent is the aforementioned artifact of the large scan region (6 μm scan), where the left and right edges of the modulus image [Figure 5(b)] appear to be less stiff due to the tip scanning away from the top of the fiber. It is unclear whether the raised bumps are surface impurities or part of the inherent structure, but they have been observed in

the KM2 Plus, Twaron, and the AuTx. For all of the defects found here, there are regions that appear at least somewhat more compliant due to the defect feature. In contrast to the KM2 Plus and Twaron, the AuTx does not appear to have a very fine, top–bottom oriented fibrillar structure. It appears that the inherent structure of the AuTx is designed to have more fibril bundles as opposed to single fibrils.

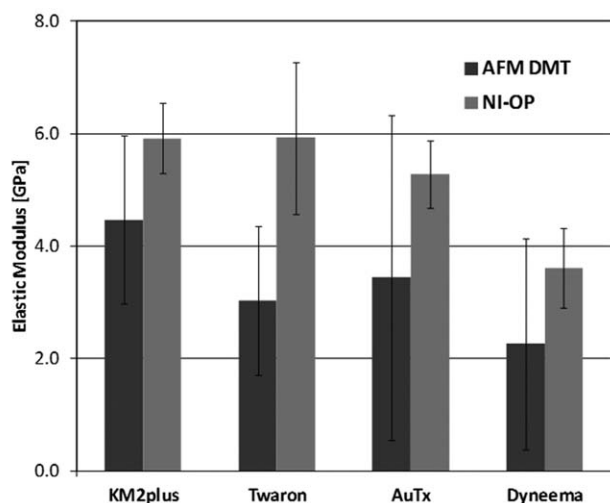


Figure 8. Averages and standard deviations of modulus values from 1 μm AFM modulus maps. Elastic modulus and standard deviation of fibers found through instrumented NI according to Oliver–Pharr model are also included (NI-OP).

Dyneema filament surfaces are generally not particularly cylindrical due to the large corrugation roughness. Figure 6 shows two pairs of $3 \times 3 \mu\text{m}$ Dyneema filament images. Figure 6(a,b) show a rugged corrugation of up–down fibrils including fibrils which exhibit a shish-kebab structure, as other researchers have also noted.^{11–13,18} The fibril corrugation is interrupted by some larger stray fibrils, 130 nm wide, which have lateral shish-kebab structure to the right and some smaller stray fibrils (20–80 nm wide, 5–50 nm tall) toward the center–left of the images which appear to have been pulled from their up–down starting points. The overall corrugation shows a variety of stiffnesses pertaining to the fibrils, and the larger stray fibrils appear to have lower (200–400 MPa) stiffness than the surrounding fibrils (overall image modulus: 778 MPa). Figure 6(c,d) also shows a corrugation plus shish-kebab structure, but is punctuated by various lakes or inclusions of amorphous low-stiffness regions, some small and round (ca., a few hundred nanometers in diameter), while others are larger and typically elongated, nearly the length of the $3 \mu\text{m}$ image and 50–400 nm across. The stiffness of these lakes is about 300–400 MPa, or about 50% of the overall image stiffness (704 MPa). The chemical identity of these regions is not known; they may be amorphous polyethylene, mineral oil, or perhaps some foreign impurity. Overall, Dyneema exhibits the most unique structure in that it is multi-directional due to its shish-kebab formation. Furthermore, Dyneema does not appear to have small or solo stray fibril regions but instead exhibits long stray bundles of fibrils. Also, the raised bumps and clusters found in the other three fibers are not found in Dyneema. Instead, Dyneema has apparently amorphous lakes or inclusions on its surface.

Overview of Local Non-Defect Surface Morphologies

Interestingly, for each of the fibers studied, most of the surfaces are covered with features or defects, while the intended flawless morphology is present on only a very low fraction of the surface. These flawless regions are so uncommon that typically

even a 1 μm zoom to a specific region is still not guaranteed to show the intended morphology. Therefore, it is important to remember that the expected surface structure found on any of these fibers will contain many defects. On the other hand, it is also valuable to show the relatively defect-free surfaces, conceivably the intended fiber morphology at the micro-/nanoscale.

Figure 7 shows a set of AFM height images (a–d) with corresponding modulus maps (e–h) for each of the fibers studied. From top to bottom they are: KM2 Plus (7a and 7e), Twaron (7b and 7f), AuTx (7c and 7g), and Dyneema (7d and 7h). These images were chosen from the tens of images collected such that they exhibit the typical fiber surface morphology with very few defects. As can be seen in the height images, the KM2 Plus (7a) and the Twaron (7b) appear to be anisotropic with fine (~ 5 –20 nm wide) features persisting in the filament direction. The anisotropy remains in the modulus maps (7e and 7f). On the other hand, the height images of the AuTx (7c) and the Dyneema (7d) appear to have large scale (100s of nanometers) anisotropy which is either large scale meso-fibrils or fibril bundles. These fibril bundles result in relatively large scale corrugation morphology, with ridges or grooves running in the filament direction, which can also be observed in the modulus maps (7g and 7h). Also present in the AuTx and the Dyneema images (7c and 7d) are smaller scale (5–20 nm) structures that appear to be isotropic or random on the AuTx surface (7c), appearing as a light-colored (high height) raised haze. These features are much more noticeable in the AuTx modulus map (7g), where they appear as a more dominant isotropic grainy structure. This structure was noted above as “regions or small islands of raised haze” in the KM2 Plus and to some extent the Twaron, and is typically more prominent near defect sites. The small scale structures on the Dyneema surface appear to populate more sparsely in the height image (7d); however, that is due to the image (7d) having the largest overall height scale, and thus contrast is lost. Upon further investigation, the Dyneema modulus map (7h) shows clearly bright and dark (stiff and compliant, respectively) regions which form a bidirectional morphology. The Dyneema modulus map clearly shows distinctly shish-kebab structures in the filament direction, especially along the left and right edges of the image. In addition, interdigitated shish-kebabs run down the middle of the image, resulting in a basket weave pattern. All in all, of these four sets of images, the Dyneema morphology qualitatively appears to be the least anisotropic (being more bi-directional) and also has the largest distances (or areas) of compliant material between stiff features. Finally, appearing in the Dyneema modulus map (7h) are small (ca., $100 \times 250 \text{ nm}$) lakes of very compliant (dark contrast) material.

Overview of DMT Contact Modulus Method for Fiber Study

The AFM DMT contact modulus method uses the DMT contact model³¹ in conjunction with a modulus mapping method³⁰ that consists of a series of small amplitude (ca., 10 nm) force–displacement curves, with an appropriate stiffness probe. Combining the DMT model with the high-frequency (ca., 2 KHz) force curve mapping technique assumes purely elastic deformations to map the stiffness of a surface, and then quantifies that stiffness by referencing a sample of

Table II. Summary of AFM Modulus Mapping Observations

Fiber	Overall fiber shape	Structure directionality with respect to fiber	Prominent compliant feature	Other distinct feature
KM2 Plus	Cylindrical/fine corrugation	Parallel	40 nm bumps, clusters	Fine fibrillar structure, random scratches
Twaron	Cylindrical/fine corrugation	Parallel	40 nm bumps, clusters	Fine fibrillar structure, random scratches
AuTx	Cylindrical/rough corrugation	Parallel and transverse	40 nm bumps, clusters	Large corrugation (braided) fibril bundles
Dyneema	Non-cylindrical/rough corrugation	Parallel and transverse	~100's nm amorphous lakes	Shish-kebab crystalline

known modulus (polystyrene). Figure 8 summarizes the AFM DMT modulus values for the various fibers tested in this study (values are also tabulated in Table I). AFM DMT values are an average from at least ten images of a $1 \times 1 \mu\text{m}$ scan size. Smaller scan regions were used in order to avoid the lower stiffness values found at the edges of the larger AFM scans, as noted previously. To benchmark these modulus values, NI was also performed on the fibers. While similar elastic behavior was expected, note that the two tests have four major differences that may lead to discrepancies in the observed modulus values. First, for NI, tests were performed at relatively large contact depths (approximately 200 nm versus ca. 5 nm for AFM DMT method). Differences in contact depths will result in measurement variability due to changes in the defect density of the surface versus the underlying “bulk” or “core” of the sample. Contact depth is also a factor to be considered when evaluating the effect of roughness and sample curvature. For shallow contact depths, the effect of even small sample roughness can be substantial. Second, NI tests utilize a much larger probe (ca., 50–200 nm radius of curvature, versus ca. 10 nm for AFM) and result in a relatively large contact region; thus, the elastic properties obtained via NI are considered less local (but still not necessarily bulk properties). Third, NI is an elastic–plastic deformation process while the AFM tests can be considered purely elastic. Fourth, the differences in these two deformation processes become even more involved when the measurement rate (or contribution of elasticity) is considered. While NI is considered to be quasi-static and uses a ramp-rate of 25 nm s^{-1} , the AFM mapping technique uses a force-curve frequency of about 2 KHz and a ramp size of approximately 10 nm. This results in a rate on the order of $40,000 \text{ nm s}^{-1}$. Therefore, although quasi-static conditions are assumed in the treatment of the data here, the values obtained may be substantially affected by the AFM force-curve (dynamic) ramp rates used. All of the modulus values are of the same order, yet the NI values are always larger than the AFM modulus values. Furthermore, the error bars (two standard deviations) of the AFM measurements are typically double the uncertainty in the NI measurements. In addition to (and in conjunction with) the caveats noted above, the uncertainty is also affected by the ca. 30 percent error inherently involved in the AFM technique.^{34–36}

The AFM DMT technique assumes a contact radius which is calculated by assuming the modulus measured on PS is 2.7 GPa. The technique also requires that the deformation of the reference measurement matches the deformation of the sample measurement. The deformation on both PS and each fiber was controlled at approximately 5 nm. However, the PS reference is extremely flat, with an RMS roughness about 1 nm. On the other hand, the fibers studied have relatively high roughness (anywhere from 1 to 100 nm) even on plane-fitted images. The roughness includes at least three length scales: (1) fibril, raised bump, and pore (very fine) corrugation; (2) fibril bundles, long trenches or scratches, and larger scratch-like feature corrugation; and (3) the cylindrical shape of the fibers themselves. In every one of these cases, the tip encounters a surface at a non-normal angle to the global sample surface. This causes the true tip-sample contact area to change. Since the DMT model used here assumes a constant tip radius (and therefore contact area), the local modulus values across an image are affected by the topography encountered. For large scan sizes, the edges of the image—where the tip encounters a large angle at the side of the fiber (vs. at the apex)—may result in a misleading stiffness value. In a similar way, long trenches and fibril bundle topography are capable of casting “shadows” onto the modulus image and contain both a high and a low modulus value dependent on the tip scan direction with respect to the local sample slope.

Effect of Defects on Measured Properties

The AFM data show some clear and distinct microstructural features or defects which could affect the fiber properties. Certainly they affect local properties but the question remains: do any of these defects affect bulk properties? In order to place these observations into greater context, the next step would be evaluation of the transverse modulus of the single filaments and single filament tensile testing. Another approach would be to determine which, if any of these surface defects contributes to the tensile strength, or the ultimate failure of a filament in tension. It is possible that large pulled out fibril bundles or long trenches are large enough to be a critical defect. Or it could be that any of these defects grow when the fiber is placed in tension. On the other hand, defect structure within the fiber could prove to be more important to the ultimate tensile strength of such fibers. Capturing the various morphologies is simply a

starting point for the study of how chemistry and processing affect morphology and therefore bulk properties of these fibers.

CONCLUSION

Morphology and local properties of four ballistic fiber types were observed using AFM and NI techniques. AFM modulus data were acquired through a force curve mapping technique using a DMT model of elastic contact with attractive interactions. Modulus values obtained from the AFM modulus mapping and the NI technique are summarized in Table I. The following observations were found upon performing 6, 3, and 1 micron scans on several samples of each filament type, and are summarized in Table II:

1. Most surfaces are not defect free.
2. Fibers are primarily anisotropic having a directionality of fibrils and/or fibril bundles in the fiber direction.
3. Fibers can have a structure transverse to the fiber direction—most prominent in Dyneema and somewhat in AuTx, but less so for KM2 Plus and Twaron.
4. All fibers have a compliant feature that is ubiquitous – for KM2 Plus, Twaron and AuTx: raised features on the order of 40 nm, randomly shaped, often forming clusters or agglomerates.
5. The compliant feature for Dyneema appears to be an amorphous region forming an inclusion or elongated lake on the surface. It is not clear what this material is for any of the fibers.
6. All fibers exhibit stray fibril bundles, having only slightly lower modulus only because they are not fixed rigidly to the surface. This is more prominent for AuTx and Dyneema.
7. All fibers exhibit stray single fibrils. In some cases, especially for KM2 Plus and Twaron, this may form various densities of a “raised haze” in the topography.
8. Dyneema exhibits a shish-kebab structure and thus is the least anisotropic of the fibers studied.

Finally, AFM modulus values obtained through the DMT model are described with respect to fibers with varying roughness and then compared with NI modulus values obtained through the conventional OP model. Values were found to be of the same order of magnitude, but the standard deviation of the AFM modulus data were typically twice as large, possibly due to the AFM's (1) locality of measurement, (2) surface sensitivity, and (3) inherent limitations which have been documented.

The observations reported here will serve as a starting point for evaluating fiber morphologies and local properties in order to better understand their effect upon bulk fiber tensile properties, especially the ultimate strength of a single filament. The techniques described in this work have the potential to lead to a better understanding of chemistry–processing–morphology–property relationships in ballistic and other specialty fibers.

ACKNOWLEDGMENTS

The authors acknowledge Stephanie Marcott, Erica Ford, Christopher Drew and Ramanathan Nagarajan of Natick Soldier Research, Development & Engineering Center for providing the fibers used in this study. KES gratefully acknowledges helpful discussions with Eric Wetzel at ARL and also discussions with Quinn P. McAllister. DPC is a contractor to ARL under contract NNL09AA00A.

REFERENCES

1. Cunniff, P. M.; Auerbach, M. A.; Vetter, E. and Sikkema, D. J. In Proceedings of 23rd Army Science Conference, Orlando, FL, **2002**; p 8.
2. Cunniff P. M. In Proceedings of 18th International Symposium on Ballistics, San Antonio, TX, **1999**; p 1303.
3. McDonough, W. G.; Holmes, G.A.; Forster, A. L.; Rice, K. D. In SAMPE 2010 Annual Technology Conference, Seattle, WA, **2010**; p 9.
4. Phoenix, S. L.; Porwal, P. K.; Shivakumar, K. *Int. J. Solids Struct.* **2003**, *40*, 6723.
5. Singletary, J.; Davis, H.; Song, Y.; Ramasubramanian, M. K.; Knoff, W. J. *Mater. Sci.* **2000**, *35*, 583.
6. Antipov, E. M.; Lebedev, Y. A.; Rebrov, A. V.; Kuptsov, S. A.; Pakhomov, P. M.; Galitsin, V. P. *Polym. Sci. Ser. A: Polym. Phys.* **2007**, *49*, 663.
7. Black, W. B. *Annu. Rev. Mater. Sci.* **1980**, *10*, 311.
8. Clements, L. L. In Handbook of Composites; Peters, S. T., Ed.; Chapman & Hall: London, **1998**; Chapter 10, p 202.
9. Dobb, M. G.; Park, C. R.; Robson, R. M. *J. Mater. Sci.* **1992**, *27*, 3876.
10. Jassal, M.; Ghosh, S. *Indian J. Fiber Text. Res.* **2002**, *27*, 290.
11. Jian, T.; Shyu, W.-D.; Lin, Y.-T.; Chen, K.-N.; Yeh, J.-T. *Polym. Eng. Sci.* **2003**, *43*, 1765.
12. Litvinov, V. M.; Xu, J.; Melian, C.; Demco, D. E.; Möller, M.; Simmelink, J. *Macromolecules* **2011**, *44*, 9254.
13. Ohta, Y.; Murase, H.; Hashimoto, T. *J. Polym. Sci., Part B: Polym. Phys.* **2005**, *43*, 2639.
14. Rebouillat, S.; Peng, J. C. M.; Donnet, J.-B. *Polymer* **1999**, *40*, 7341.
15. Shim, V. P. W.; Lim, C. T.; Foo, K. J. *Int. J. Impact Eng.* **2001**, *25*, 1.
16. Slugin, I. V.; Sklyarova, G. B.; Kashirin, A. I.; Tkacheva, L. V. *Fibre Chem.* **2006**, *38*, 25.
17. Smith, P.; Lemstra, P. J. *J. Mater. Sci.* **1980**, *15*, 505.
18. Smook, J.; Pennings, J. *Colloid. Polym. Sci.* **1984**, *262*, 712.
19. Tikhonov, I. V.; Tokarev, A. V.; Shorin, S. V.; Shchetinin, V. M.; Chernykh, T. E.; Bova, V. G. *Fibre Chem.* **2013**, *45*, 1.
20. Young, R. J.; Lu, D.; Day, R. J.; Knoff, W. F.; Davis, H. A. *J. Mater. Sci.* **1992**, *27*, 5431.
21. Zachariades, A. E.; Kanamoto, T. *Polym. Eng. Sci.* **1986**, *26*, 658.
22. Cheng, M.; Chen, W.; Weerasooriya, T. *Int. J. Solids Struct.* **2004**, *41*, 6215.
23. Hudspeth, M.; Nie, X.; Chen, W. *Polymer* **2012**, *53*, 5568.
24. Kitagawa, T.; Yabuki, K.; Young, R. J. *Polymer* **2001**, *42*, 2101.
25. Lim, J.; Zheng, J. Q.; Masters, K.; Chen, W. W. *J. Mater. Sci.* **2010**, *45*, 652.
26. Lim, J.; Zheng, J. Q.; Masters, K.; Chen, W. W. *Int. J. Impact Eng.* **2011**, *38*, 219.
27. Sanborn, B. D.; Weerasooriya, T. *ARL Technical Report* **2013**, ARL-TR-6465, p 26.
28. Tan, V. B. C.; Zeng, X. S.; Shim, V. P. W. *Int. J. Impact Eng.* **2008**, *35*, 1303.

29. Yeh, W.-Y.; Young, R. J. *Polymer* **1999**, *40*, 857.
30. Peakforce QNM User Guide 004-1036-000 Rev. E, 2011, Bruker; p 84.
31. Derjaguin, B. V.; Muller, V. M.; Toporov, Y. P. *J. Colloid. Interf. Sci.* **1975**, *53*, 314.
32. Cole, D. P.; Strawhecker, K. E. *J. Mater. Res.* **2014**, *29*, 1104.
33. Oliver, W. C.; Pharr, G. M. *J. Mater. Res.* **1992**, *7*, 1564.
34. Schön, P.; Dutta, S.; Shirazi, M.; Noordermeer, J.; Vancso, J. G. *J. Mater. Sci.* **2011**, *46*, 3507.
35. Dokukin, M. E.; Sokolov, I. *Langmuir* **2012**, *28*, 16060.
36. Strawhecker, K. E.; Hsieh, A. J.; Chantawansri, T. L.; Kalcioğlu, Z. I.; Van Vliet, K. J. *Polymer* **2013**, *54*, 901.